Atypical exciton-phonon interactions in WS_2 and WSe_2 monolayers revealed by resonance Raman spectroscopy

E. del Corro,[1†‡] A. Botello-Méndez,[2‡] Y. Gillet,[2] A. L. Elias,[3] H. Terrones,[4] S. Feng,[3] C. Fantini,[1] Daniel Rhodes,[5] N. Pradhan,[5] L. Balicas,[5] X. Gonze,[2] J-C Charlier,[2] M. Terrones,[3,6] and M. A. Pimenta.[1]*

[1]Departamento de Fisica, Universidade Federal de Minas Gerais (UFMG), Caixa Postal 702, 30123-970 Belo Horizonte, Brazil. [2]Institute of Condensed Matter and Nanosciences (IMCN), Université catholique de Louvain (UCL), Chemin des Etoiles 8, bte L7. 03. 01, 1348 Louvain-la-Neuve, Belgium. [3]Department of Physics and Center for 2-Dimensional and Layered Materials, Pennsylvania State University, Pennsylvania, PA 16802, USA. [4]Department of Physics, Applied Physics, and Astronomy, Rensselaer Polytechnic Institute, Troy, NY12180-3590, USA. [5]National High Magnetic Field Lab, Florida State University, 1800 E. Paul Dirac Dr. Tallahassee, FL 32310, USA. [6]Department of Chemistry and Department of Materials Science & Engineering, The Pennsylvania State University, University Park, PA 16802, USA

Abstract

Resonant Raman spectroscopy is a powerful tool for providing information about excitons and exciton-phonon coupling in 2D materials. We present here resonant Raman experiments of single-layered WS_2 and WSe_2, using more than 25 laser lines. The Raman excitation profiles of both materials show unexpected differences: all Raman features of WS_2 monolayers are enhanced by the first-optical excitations (with an asymmetric response for the spin-orbit related X_A and X_B excitons), whereas Raman bands of WSe_2 are not enhanced at $X_{A/B}$ energies. Such an intriguing phenomenon is addressed by DFT calculations and by solving the Bethe-Salpeter equation. These two materials are very similar: they prefer the same crystal arrangement, and their electronic structure is akin, with comparable spin-orbit coupling. However, we reveal that WS_2 and WSe_2 exhibit quite different exciton-phonon interactions. In this sense, we show that the interaction between X_C and X_A excitons with phonons explains the different Raman responses of WS_2 and WSe_2 and the absence of Raman enhancement for the WSe_2 modes at $X_{A/B}$ energies. These results reveal unusual exciton-phonon interactions and open new avenues for understanding the 2D materials physics, where weak interactions play a key role coupling different degrees of freedom (spin, optic, electronic).

Keywords: bidimensional materials, transition metal dichalcogenides, resonant Raman spectroscopy, first-principles calculations, exciton-phonon interaction.

The field of two dimensional (2D) materials has grown incredibly fast due to the fascinating and outstanding physical properties of these atom-thick layers. In particular, 2D transition metal dichalcogenides (TMDs) have been placed at the center of the stage along with graphene, with MoS_2 being the most representative prototype [1]. Furthermore, monolayers of semiconducting TMDs are very attractive for the development of novel applications in optics, optoelectronics, and magneto-

optoelectronics [2-4]. However, before any of these far reaching applications can be unambiguously targeted, proper characterization and clear understanding of their properties, particularly of the coupling between different physical phenomena (e.g., electronic and optical, or optical and vibrational, or the three of them), must be achieved.

Concerning the electronic structure of these systems, monolayered WS_2 and WSe_2 exhibit a direct band gap at the corners of the Brillouin zone (*k*-points K and K') [5]. This is in contrast with their bulk counterpart, where the smallest gap is indirect between K and a point Λ (between K and M) [5, 6]. Another unique aspect of the electronic structure of this material is the significant spin-orbit coupling (SOC) which lifts the degeneracy at the K and K' points, thus leading to a large splitting of the valence band of *ca.* 400 meV and 450 meV for WS_2 and WSe_2, respectively [5]. The weak dielectric screening of the Coulomb interaction is responsible for a strong exciton binding energy and, therefore, excitonic states dominate the absorption spectrum of these systems [7, 8]. For WS_2, the absorption spectra is characterized by three excitonic states commonly labeled as X_A, X_B and X_C with absorption peaks at *ca.* 2.0, 2.4 and 2.8 eV, respectively [7-9]. The X_A and X_B peaks are associated with the first (1s) excitation of the direct band transition at K, with their difference in energy ($|E(X_A)-E(X_B)|$) directly related to the SOC splitting. X_C is often attributed to practically degenerate transitions near Γ. Recent measurements of the electronic gap yield exciton binding energies of 0.7 eV for the X_A and X_B and 1.3 eV for X_C [10]. Concerning the binding energy for the X_A and X_B, some controversy can be found in the literature, and an alternative value of 0.32 eV has been reported [7]. In addition, higher orders in the excitonic Rydberg series of X_A and X_B have been identified in differential reflection experiments, with the most prominent 2s resonance of the A exciton ($X_A^{(2s)}$) located at 2.18 eV [7, 9]. Qualitatively, WSe_2 monolayers are very similar, with values of *ca.* 1.7, 2.1, and 2.4 eV for the X_A, X_B, and X_C, respectively [8, 11]. Higher order 2s excitations have been found at 1.8 and 2.3 eV for $X_A^{(2s)}$ and $X_B^{(2s)}$ excitons, respectively [11].

Monolayered 2H-TMDs of WS_2 and WSe_2 form 2D crystals with a sandwich-like structure composed of three triangular sublattices, where the metal sits in one sublattice between the chalcogens forming two opposed tetrahedrons arranged in such a way that they all form a hexagonal network when viewed from the top. Both systems belong to the same symmetry point group, D_{3h}, and exhibit a total of 9 phonon branches. Three zone-center modes (**q**=0) are Raman active and belong to the A'_1, E' and E'' representations [12]. However, in the backscattering geometry where the incident light direction is perpendicular to the basal plane, only two Raman active first order bands are observed, labeled A'_1 and E' bands. Thus, the typical first-order Raman spectrum of these compounds is dominated by A'_1 and E' modes. Along with the first-order Raman active modes, a number of features have been identified in the spectrum of WS_2 and WSe_2 which are associated with second-order processes, such as combinations or overtones of phonons with finite wavevectors (**q**≠0**)** usually located at the corners and edges of the Brillouin zone. These second-order features were already observed in bulk TMDs [13] but only recently a detailed explanation of their origin was proposed for monolayer WS_2 and MoS_2 [6, 14].

Raman spectroscopy was shown to play a key role in the identification of 2D materials; for example, it can be used to distinguish and identify the number of layers in graphene and TMDs [15-18]. Moreover, as mentioned, TMDs containing Mo or W and S or Se display a direct to indirect band-gap transition when going from monolayer towards the bulk [19], thus affecting the resonant Raman conditions [6, 18, 20-22]. However, the analysis of the Raman and resonant Raman response of these materials offers more information that needs to be understood, since light scattering due to phonons reveals evidence about the interplay between electronic, optical and vibrational properties. Resonant Raman spectroscopy has been proved to provide evidence concerning exciton-phonon coupling [23], spin orbit coupling (SOC) [24] or lifetime of the excitonic states [22], among others. The resonant Raman spectra of bulk TMDs (2H-MoS_2, WS_2, WSe_2, and MoS_2) have been studied in the past [25-27]. For bulk MoS_2 and WS_2 it was observed that the resonant excitation profile, *i.e.* Raman intensity *vs*. excitation energy, (REP) behaves

differently for the out-of-plane and in-plane modes (A^1_g and E^1_{2g}, respectively), since only the A^1_g band resonates at all energies corresponding to the excitonic states; such behavior is indicative of a symmetry dependence of the exciton-phonon coupling that governs the REP. More recently, resonant Raman studies of WSe_2 and MoS_2 systems with different number of layers have been performed and can be found in the literature [20, 22].

In this letter we compare the resonant Raman response of single layered WS_2 and WSe_2, using up to 25 excitation energies in the visible range, and we observe quite different and intriguing behavior for each material. For monolayer WS_2, the main first and second-order Raman features (E', A_1', 2LA(M)) are enhanced for laser energies corresponding to the first optical excitations (X_A, X_B and X_C). In contrast, the behavior of monolayer WSe_2 is found to be more complex. On one hand, the REP of first and second- order modes differs, and on the other hand, the normal Raman modes, E', A_1', show no Raman enhancement in the energy region of the first optical excitations. Such a difference has not been previously reported and in this work we further investigate it with the aid of state-of-the-art first-principles calculations at two different levels, starting with density-functional-theory (DFT), and then by solving the Bethe-Salpeter equation for the excitonic states.

Figure 1 shows the Raman spectrum of WS_2 and WSe_2 monolayers measured with the 488 nm excitation wavelength. The two first-order modes of the Raman spectrum, E' and A_1', are present for monolayered WS_2 around 356 and 418 cm^{-1}; but, for monolayered WSe_2 they are degenerated in frequency, appearing around 250 cm^{-1}.[28] For both materials, additional second-order Raman contributions can be observed, and the most prominent one is ascribed to the 2LA(M) band, originated from a second-order double resonant process involving two longitudinal acoustic (LA) phonons close to the M point of the Brillouin zone [18]. However, when using different excitation lines (Figure 2) it is observed (especially in WSe_2) that the 2LA band is formed by more than one contribution, very close in frequency. The origin of these 2LA Raman features was recently reported for MoS_2, and authors

assigned these contributions to LA phonons at and in between the K and M points of the Brillouin zone[29]. In order to obtain the band intensities, the 2LA band of WS_2 and WSe_2 is fitted to one and two Lorentzian functions, respectively. In the case of WS_2, this band appears at slightly lower frequency than the E' mode; and for WSe_2, the 2LA contributions are observed at higher frequency, around 260 and 263 cm^{-1}.

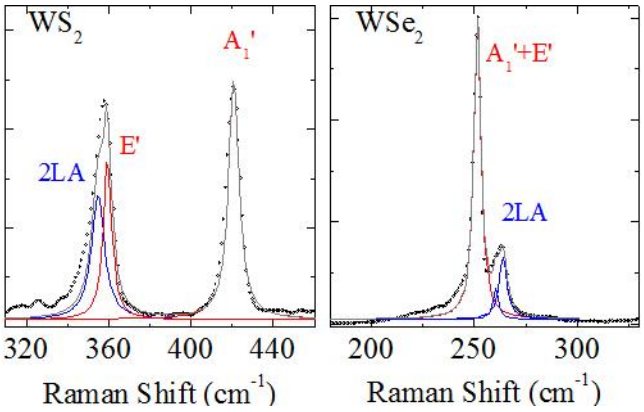

Figure 1. Raman spectra of monolayered WS_2 and WSe_2 (dots). The spectra are measured with the 488.0 nm excitation wavelength. Fitting of the spectra is shown by a solid grey line. First and second-order Raman contributions are depicted by red and blue Lorentzian fitting functions, respectively.

Figure 2 plots selected Raman spectra of monolayered WS_2 and WSe_2 recorded with excitation wavelengths within the visible range. The relative intensities of the first and second-order contributions dramatically change with the excitation energy. A resonant Raman process occurs when the energy of the incident or the scattered photon matches the energy of an optical transition. As already mentioned, the TMDs exhibit excitonic band gaps in the visible range; therefore, when the incident and scattered photons are in resonance with excitonic transitions, the Raman scattering intensity increases abruptly. For the analysis of such resonant processes, the spectra in Figure 2 are fitted with a sum of Lorentzian functions (see Supporting Information). The intensities of the Raman peaks of WS_2 and WSe_2 were normalized by the intensity of the Si Raman peak of the substrate, at 521 cm^{-1}, considering its excitation energy dependence[30]. There is a correction in the relative intensities of the TMDs and Si

peaks due to multiple optical interferences in the SiO_2 layer. However, as discussed by Carvalho et al. for MoS_2 samples[22], this correction does not affect our main results and conclusions. In Figures 3 and 4 we present the REP for WS_2 and WSe_2 monolayers, respectively.

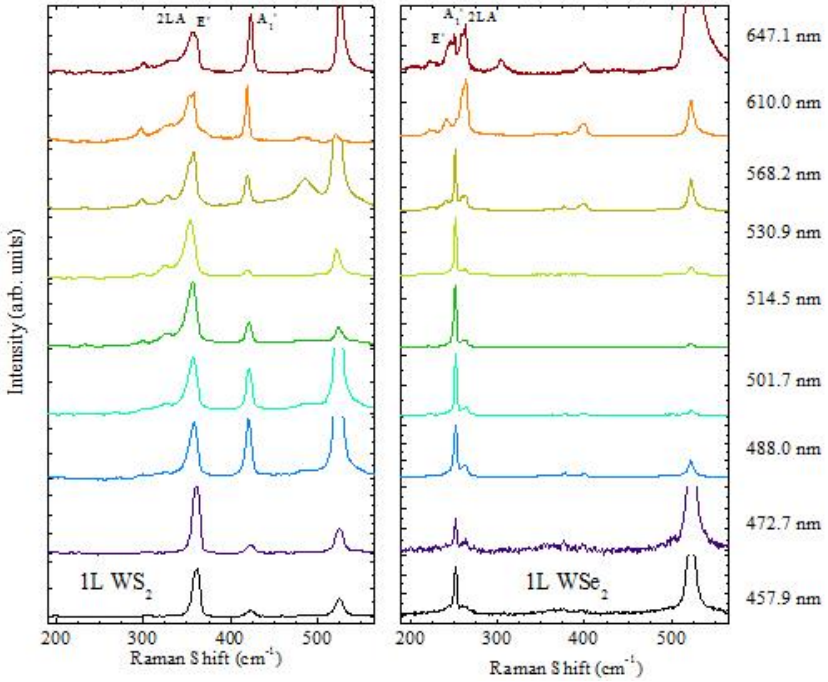

Figure 2. Resonant Raman spectra of TMDs. Selected Raman spectra of monolayered WS_2 and WSe_2 samples registered with different excitation wavelengths. The spectra intensity is arbitrarily set to improve the clarity of the results. The laser energy (indicated by the color of the spectra) is showed in nm on the right.

The REPs of the A_1', E' and 2LA Raman bands of monolayered WS_2 (Figure 3) show three maxima of Raman intensity enhancement, in good agreement with previous optical absorption results also performed in monolayers [31]. Two enhancements appear around 2.0 and 2.4 eV, corresponding to X_A and X_B excitonic states. In addition, a third enhancement is observed at *ca.* 2.7 eV, and it is caused by the resonance with the X_C absorption. An interesting behavior is observed when comparing the REP of the first-order modes: while the E' band shows a REP with two peaks (at X_A and X_B energies) of similar intensity, the REP of the A_1' band displays a peak corresponding to the X_A exciton five times

higher than that of the X_B. Such behavior reveals a symmetry breaking between the X_A and X_B exciton-phonon interaction, caused by a non-trivial interaction between the spin, electronic and vibrational degrees of freedom.

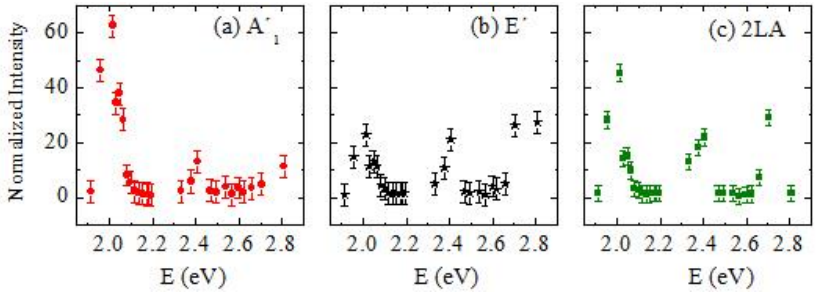

Figure 3. Experimental REP of WS_2. Resonant excitation profiles of the Raman bands A_1´, E´ and 2LA of monolayered WS_2. Each of the REP shows three enhancements at *ca*. 2.0, 2.4 and 2.7 eV, corresponding to X_A, X_B and X_C exciton energies, respectively. The intensity of the Raman enhancement at these exciton energies differs for each Raman contribution, as previously observed for MoS_2 [22].

The analysis of the REP of WSe_2 is slightly more complex than that of WS_2. Within the excitation range studied in this work, the Raman spectrum should show enhancements at *ca.* 2.1 and 2.4 eV corresponding to X_B and X_C, respectively (note that the X_A exciton is out of the energy range considered in this work). Surprisingly, in Figure 4 we observe that only the 2LA band behaves as expected, showing the mentioned enhancements. In contrast, the first-order Raman bands only exhibit a single intensity enhancement around 2.42 eV, associated to the X_C transition. This resonance of WSe_2 REP at 2.42 eV has been previously associated to the X_B (2s) transition at 2.3 eV [20]. However, in view of the low quantum efficiency observed for this 2s transition as revealed from its low reflection, [11] such an alternative interpretation can be ruled out. Similar studies were performed by the authors in WSe_2 samples with more than one layer; [20] and for the thicker samples the same intriguing behavior was observed: the absence of enhancement associated with X_B transition. Moreover, resonant Raman

spectra were recorded in the near IR excitation range, X_A transition, but the Raman signal was negligible for all the WSe_2 samples (single to tri-layered and bulk).

The differences observed between the REP of WS_2 and WSe_2 are rather unexpected - there is no *a-priori* reason for these systems to behave differently, since the two crystal and electronic structures are quite similar. Moreover, the different REP showed by the first and second-order modes of WSe_2 is startling. In order to address such an intriguing behavior, theoretical calculations using density functional theory (DFT) were performed, followed by solving the Bethe-Salpeter equation (BSE) for the excitonic states, as presented in the following section.

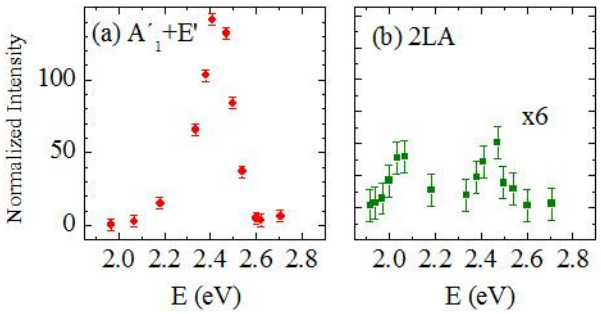

Figure 4. Experimental REP of WSe_2. Resonant excitation profiles of the first-order Raman bands, $A_1´$ + E´, and of the second-order 2LA band of monolayered WSe_2. For the first-order vibrational modes the REP present a single enhancement at *ca*. 2.4 eV, corresponding to X_C. The 2LA band REP shows two enhancements at *ca*. 2.1 and 2.4 eV, in resonance with the X_B and X_C exciton energies. Two main contributions to the 2LA band are separated in the fitting procedure; (c) shows the REP of the 2LA contribution at 260 cm^{-1}, see Supporting Information for the REP of the 2LA contribution at 263 cm^{-1}.

In the simplest picture, the REP should follow the absorption spectrum, since as more light is absorbed, more phonons are excited. In this sense, the computation of the Fermi Golden rule (FGR) based on DFT and assuming the matrix elements to be constant, would be the first approach. The advantage of this approach is that SOC is included, and that second-order Raman processes are considered[19]. More details concerning this approach are found in the Supporting Information and the theoretical REP of the

2LA band of both materials is presented. But as observed in the Supporting Information (Figure S4), this computation method does not offer a good account for the difference in both materials; thus, the discrepancy must come from the coupling between radiation, electrons and phonons (*i.e.* the coupling matrices).

Instead, we have considered the Raman scattering as the result of the change in polarizability in the scattering crystal subject to vibrations. Thus, we have computed the REP from the derivative of the dielectric function ϵ within the BSE approximation to account for the excitonic properties of these materials. Recall that the dielectric function describes the response to an external excitation with energy (ξ_L) considering all excitonic states (E_λ) and their oscillator strengths (f_λ). It contains all the information regarding the optical properties. The expression of the dielectric function and its first-order derivative with respect to a phonon displacement, x, are given respectively by:

$$\epsilon(\xi_L) = \sum_\lambda \frac{f_\lambda(\vec{x})}{\xi_\lambda - E_\lambda(\vec{x}) - i\gamma} \qquad \text{Eq. 1}$$

$$\left|\frac{d\epsilon}{d\vec{x}}(\xi_L)\right|^2 = \left|\sum_\lambda \frac{f_\lambda(\vec{x}) E'_\lambda(\vec{x})}{(\xi_L - E_\lambda(\vec{x}) - i\gamma)^2} + \frac{f'_\lambda(\vec{x})}{\xi_L - E_\lambda(\vec{x}) - i\gamma}\right|^2 \qquad \text{Eq. 2}$$

The advantage of computing the REP from BSE is that the interaction matrix elements are derived from first principles, with the caveat of losing the description of the spin orbit interaction[31]. Since the objective is to address the difference in the Raman response of these very similar materials, we focus on the behavior of X_A and X_C as a function of the characteristic displacement of the A'_1 phonon mode, via finite differences. The calculation of second-order Raman intensities requires the evaluation of second-order derivatives of the dielectric function with respect to phonon displacements on a dense q-point grid. These calculations within the BSE framework are to-date beyond the computational resources and we therefore restrict our analysis to the first-order Raman bands in the following paragraphs.

Dashed lines in Figure 5 show the response of ϵ to A'_1 displacements for WS_2 and WSe_2. The intensity is normalized to X_C and weighted with respect to Si REP[32] to simulate the experimental conditions. We can observe that the BSE calculations of $d\epsilon/dx$ reveal an enhancement corresponding to the X_A exciton for WS_2 whereas almost no enhancement is present in WSe_2 at the mentioned analogous excitonic energy. Accordingly to this finding, a similar behavior is expected for exciton X_B, which would match the experimental observations (no enhancements corresponding to X_B excitons in monolayered WSe_2). In the case of WSe_2 there is an agreement between theory and experiment for the X_C excitation energy, not observed for WS_2; however, this agreement is rather a coincidence, since an accurate evaluation of the relative position of the excitons would require self-consistent quasiparticle calculations which are out of the scope of this work).

From inspection of Eq. 2 an insight on the origin of the difference between the two materials can be obtained. The values of E_λ and f_λ, are obtained from the diagonalization of the excitonic Hamiltonian and consequently, the derivatives E'_λ, f'_λ can be obtained for each excitation state individually using finite differences. Therefore, the **f**irst term of Eq. 2 will hold the most important contribution to the REP due to the squared Lorentzian function, thus being $f_\lambda E'_\lambda$ the most significant factor. The values of this product $f_\lambda E'_\lambda$ are summarized in Table 1 under the BSE column. It is interesting to note that the sign of the product is due to the fact that $E'_{XA} > 0$ and $E'_{XC} < 0$ for the two materials. In addition, the calculated $f_\lambda E'_\lambda$ at the X_C energy is one order of magnitude larger than that at X_A in WSe_2, while it is only *ca.* 3 times larger for WS_2. The difference between the two materials is even more important once the intensities are considered, as they are proportional to the square derivatives (see Supporting Information for further details). This analysis reveals that the differences in the REP of WS_2 and WSe_2 has its origin in the different matrix elements $f_\lambda E'_\lambda$ (note that f_λ was already found to be different for WS_2 and WSe_2) [9]. The ratio of $f_\lambda E'_\lambda$ between the X_C and X_A differs for both materials explaining the unobserved enhancement of the Raman intensity for the first order modes of WSe_2 at $X_{A/B}$ energies.

Table 1. Main contribution to the Raman intensity matrix elements $f_\lambda E'_\lambda$. The values were computed either from finite differences of the dielectric function with excitonic effects (BSE) or fitted from the experimental data using the square of the first term of Eq. 2. The values are normalized with respect to the X_C peak of the A'_1 mode.

		$f_\lambda E'_\lambda$ [A'_1 mode]		$f_\lambda E'_\lambda$ [E' mode]
		BSE	*fit*	*fit*
WS_2	X_A	173.69	0.71	0.28
	X_B	-	0.36	0.30
	X_C	-549.87	-1.00	-1.17
WSe_2	X_A	161.83	-	
	X_B	-	-	
	X_C	-1591.24	-1.00	

Following this model, the bare experimental data has been normalized and fitted to a function of the square of the first term of Eq. 2 taking into account the effect of the substrate (see Methods). The fitted values are normalized to the X_C peak of the A'_1 mode due for comparison with the BSE data. Here, we considered the bare excitonic states (i.e., without the effect of the substrate) within an energy window of 0.05 eV around the maximum values of f_λ associated with X_A and X_C. Note that the sign of $f_\lambda E'_\lambda$ has little impact in the fitting procedure; however, it has been kept to conserve the physical difference in the response at the diverse excitation energies. The data collected in Table 1 under the fit columns shows qualitative agreement in the tendency of the ratio between the X_C and X_A with respect to the BSE calculations for the A'_1 mode. The E' mode values, also normalized to X_C of the A'_1 mode, reflect the different relative coupling with the X_C exciton as described recently for MoS_2 [22]. The resulting fitted curves are displayed as solid lines in Figure 5 in comparison with experimental results, where the effect of the substrate is now taken into account. While the WSe_2 data provided little information (due to the unobserved enhancements), the WS_2 fitted values reported in Table 1, provide an idea of the

relative exciton-phonon-(spin) interaction for the different phonon and exciton modes, since $f_\lambda E'_\lambda$ contains the most relevant information of the matrix elements of these interactions contributing to the Raman REP.

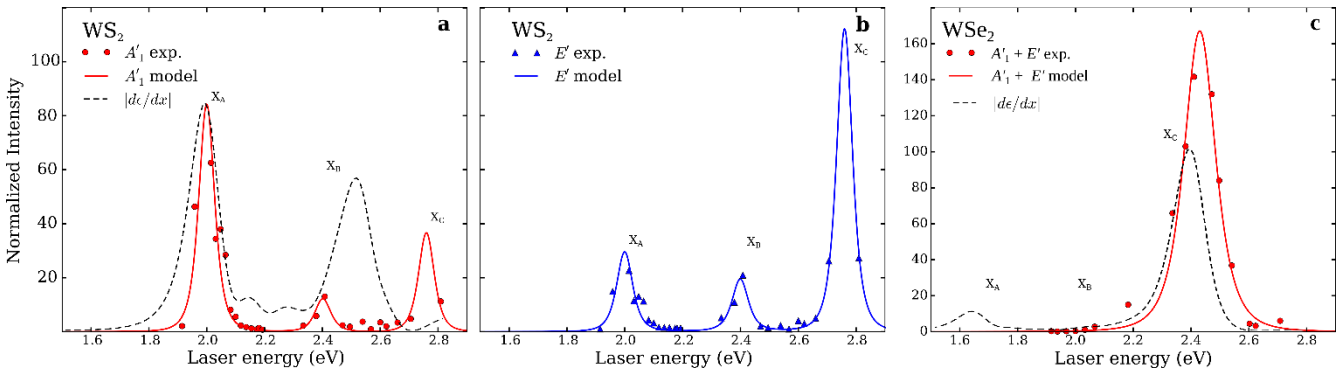

Figure 5. Experimental resonant excitation profiles for the first-order Raman bands of monolayered WS_2 and WSe_2. Dashed black lines represent the REPs obtained by means of first-principles DFT-based Bethe Salpeter calculations, as the derivative with respect to displacement of the dielectric function for the A_1' mode. Solid colored lines represent the fitting of the experimental data according to Eq. 2.

In conclusion, in this work we studied the resonance Raman response of WS_2 and WSe_2 monolayers, both experimentally, using up to 25 laser lines in the visible range and, theoretically, using state-of-the-art first-principles calculations at two different levels: density-functional-theory (DFT) and Bethe-Salpeter equation for the excitonic states. Concerning monolayered WS_2, the experimental Raman REP exhibits an asymmetric response for X_A and X_B. Interestingly, the Raman REP of the first-order modes of WSe_2 does not display the expected enhancement at the X_A and X_B exciton energy, in contrast with WS_2. Despite WS_2 and WSe_2 are nearly the same, they show a different exciton-phonon interaction, which leads to a different ratio of $f_\lambda E'_\lambda$ between X_A and X_C excitons, explaining the different REP shown by both materials. The results presented here unveil unexpected physical phenomena of WS_2

and WSe_2 monolayers, which are related to the interactions between the optical, magnetic and vibrational properties of two-dimensional TMDs, and are relevant for potential applications. Our study should motivate further experimental and theoretical advancement for the understanding of the physics of two-dimensional materials, in which the weak screening plays a very important role to couple different degrees of freedom (spin, optic, electronic).

METHODS

Experimental details

Sample preparation. Monolayered WS_2 samples synthesis is extensively described elsewhere [33]. Briefly, the sample consists of CVD grown triangular islands obtained by a two-step approach of thermal evaporation of tungsten trioxide (WO_3) onto Si/SiO_2 wafers followed by sulfurization at 800 degrees. The islands present single crystal domains of about 30 μm^2 in area with a high degree of crystallinity. Within a single island we can distinguish (by atomic force microscopy, AFM) the existence of two regions, the monolayer margins and the nucleation center composed by few layered WS_2. The size of the nucleation center composed of few layers material varies from one island to others; for this study a triangular island with a nucleation center smaller than 4 μm^2 was selected in order to ensure that the Raman characterization corresponded exclusively to the monolayer region. The monolayered WSe_2 sample was obtained by mechanical exfoliation of WSe_2 crystals produced using the chemical vapor transport (CVT) method with iodine as transport agent. The thickness of the studied flake was analyzed by AFM, which confirmed the existence of a single layer sample (0.8 nm height) with an area larger than 40 μm^2.

Raman microscopy

The micro-Raman measurements were performed in both triple monochromator spectrometers, DILOR

XY and Horiba T64000. Different laser sources (Ar/Kr, Ti/sapphire and a dye laser with Rhodamine 6G and DCM) were used in order to excite the sample in a wide energy range from 457.9 to 770.0 nm. A back scattering geometry at room temperature was used and the laser power was kept below 0.6 mW to avoid sample damage. The accumulations times varied depending on the excitation energy, ranging from 1 to 20 minutes. The laser spot diameter is about 2 μm using the 100x objective, which ensures sampling regions more than 20 times smaller than the flake areas.

Calculation details

The Fermi Golden Rule (FGR) approximation was computed from first principles calculations using the full-potential density-functional-theory (DFT) package EXCITING [34] in which the wavefunctions are expanded in terms of linearized augmented plane-waves. The generalized gradient approximation for the exchange correlation was used, and the $\sigma.L$ term was added to the Hamiltonian in order to describe the spin-orbit coupling. A dense 48x48 k-point grid, and a scissor operator to reproduce the optical gap were used. For the calculation of the optical properties, a pseudo-potential plane-wave approach (Abinit code [35]) was preferred because of the guarantee of a complete basis set, which is particularly important and difficult to converge for optical properties. The caveat, however, is the lack of SOC implementation for the optical properties. Within this approximation, the monolayer systems were simulated in a box with a 50Å separation between images in the perpendicular direction to the plane. A dense 32x32 k-point grid and 300 bands were used to compute the screening, and a γ broadening of 0.05 and 0.07 Ha were used to reproduce the experimental measurements. For the finite difference calculations, displacements with amplitudes of 0.01 and 0.005 Å were considered, and were verified to be in the linear regime. The fitting procedure presented in Table 1 was carried out as follows: the experimental data was first normalized and subsequently multiplied by the Si REP [32] to get the bare intensities; then, so normalized data were fitted to a function taking into account the square of the first element of Eq. 2 and finally renormalizing to the X_C peak of the A'_1 band.

AUTHOR INFORMATION

Corresponding author

* edelcorro@quim.ucm.es

Present Address

† J. Heyrovsky Institute of Physical Chemistry of the Academy of Sciences of the Czech Republic.

Author Contribution

‡ These authors contributes equally to this work.

ACKNOWLEDGEMENTS

This work was partially supported by the Brazilian Nanocarbon Institute of Science and Technology (INCT/Nanocarbono), Fapemig, CNPq. M.T. and L.B. acknowledge the financial support from the MURI project award No ARO-W911NF-11-1-0362. Concerning the sample preparation, M.T. also acknowledges the MURI project award No AFOSR-FA9550-12-1-0471 and support from the National Science Foundation: 2DARE-EFRI 1542707 and EFRI-1433311 (A.L.E. and H. T.). A.B.-M., Y.G., X.G. and J.-C.C. acknowledge financial support from the National Fund for Scientific Research (F.R.S.-FNRS) of Belgium. This research is directly connected to the ARC on « Graphene StressTronics » sponsored by the Communauté Française de Belgique and the Graphene Flagship funded by the European Union Seventh Framework Programme. Computational resources were provided by the Consortium des Équipements de Calcul Intensif, funded by F.R.S.-FNRS and the Tier-1 supercomputer of the Fédération Wallonie-Bruxelles, infrastructure funded by the Walloon Region under the grant agreement n°1117545.

COVERT ART

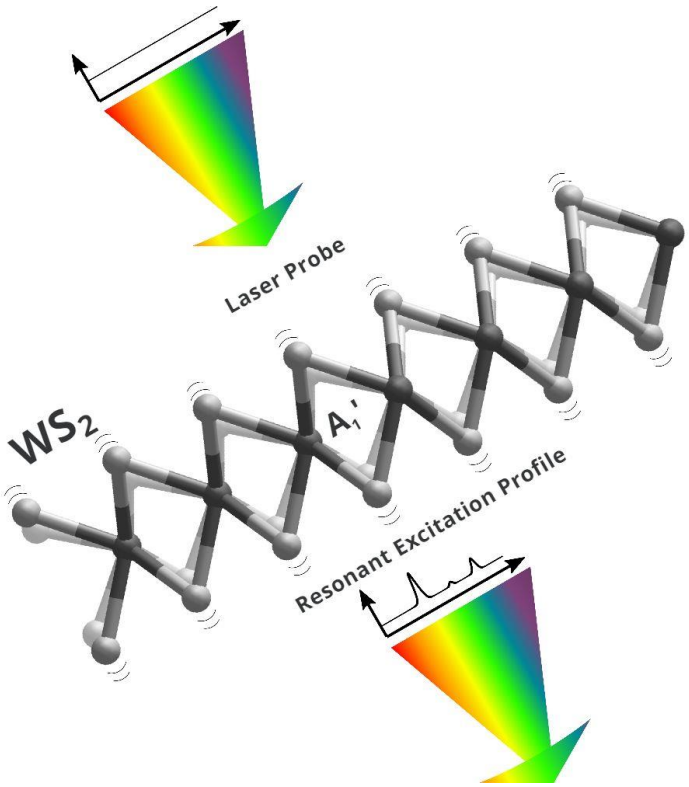

REFERENCES

1. Novoselov, K. S.; Jiang, D.; Schedin, F.; Booth, T. J.; Khotkevich, V. V.; Morozov, S. V.; Geim, A. K. *P Natl Acad Sci USA* **2005,** 102, (30), 10451-10453.

2. Radisavljevic, B.; Radenovic, A.; Brivio, J.; Giacometti, V.; Kis, A. *Nat Nanotechnol* **2011,** 6, (3), 147-150.

3. Lee, H. S.; Min, S. W.; Chang, Y. G.; Park, M. K.; Nam, T.; Kim, H.; Kim, J. H.; Ryu, S.; Im, S. *Nano Lett* **2012,** 12, (7), 3695-3700.

4. Zeng, H. L.; Dai, J. F.; Yao, W.; Xiao, D.; Cui, X. D. *Nat Nanotechnol* **2012,** 7, (8), 490-493.

5. Roldan, R.; Silva-Guillen, J. A.; Lopez-Sancho, M. P.; Guinea, F.; Cappelluti, E.; Ordejon, P. *Ann Phys-Berlin* **2014,** 526, (9-10), 347-357.

6. Zhao, W. J.; Ghorannevis, Z.; Amara, K. K.; Pang, J. R.; Toh, M.; Zhang, X.; Kloc, C.; Tan, P. H.; Eda, G. *Nanoscale* **2013,** 5, (20), 9677-9683.

7. Chernikov, A.; Berkelbach, T. C.; Hill, H. M.; Rigosi, A.; Li, Y. L.; Aslan, O. B.; Reichman, D. R.; Hybertsen, M. S.; Heinz, T. F. *Phys Rev Lett* **2014,** 113, (7), 076802.

8. Li, Y. L.; Chernikov, A.; Zhang, X.; Rigosi, A.; Hill, H. M.; van der Zande, A. M.; Chenet, D. A.; Shih, E. M.; Hone, J.; Heinz, T. F. *Phys Rev B* **2014,** 90, (20), 205422.

9. Hill, H. M.; Rigosi, A. F.; Roquelet, C.; Chernikov, A.; Berkelbach, T. C.; Reichman, D. R.; Hybertsen, M. S.; Brus, L. E.; Heinz, T. F. *Nano Lett* **2015,** 15, (5), 2992-2997.

10. Ye, Z. L.; Cao, T.; O'Brien, K.; Zhu, H. Y.; Yin, X. B.; Wang, Y.; Louie, S. G.; Zhang, X. *Nature* **2014,** 513, (7517), 214-218.

11. He, K. L.; Kumar, N.; Zhao, L.; Wang, Z. F.; Mak, K. F.; Zhao, H.; Shan, J. *Phys Rev Lett* **2014,** 113, (2), 026803.

12. Molina-Sanchez, A.; Wirtz, L. *Phys Rev B* **2011,** 84, (15), 155413.

13. Chen, J. M.; Wang, C. S. *Solid State Commun* **1974,** 14, (9), 857-860.

14. Golasa, K.; Grzeszczyk, M.; Leszczynski, P.; Faugeras, C.; Nicolet, A. A. L.; Wysmolek, A.; Potemski, M.; Babinski, A. *Appl Phys Lett* **2014,** 104, (9), 092106.

15. Ferrari, A. C.; Meyer, J. C.; Scardaci, V.; Casiraghi, C.; Lazzeri, M.; Mauri, F.; Piscanec, S.; Jiang, D.; Novoselov, K. S.; Roth, S.; Geim, A. K. *Phys Rev Lett* **2006,** 97, (18), 187401.

16. Chakraborty, B.; Matte, H. S. S. R.; Sood, A. K.; Rao, C. N. R. *J Raman Spectrosc* **2013,** 44, (1), 92-96.

17. Pimenta, M. A.; del Corro, E.; Carvalho, B. R.; Fantini, C.; Malard, L. M. *Accounts of Chemical Research* **2015,** 48, (1), 41-47.

18. Berkdemir, A.; Gutierrez, H. R.; Botello-Mendez, A. R.; Perea-Lopez, N.; Elias, A. L.; Chia, C. I.; Wang, B.; Crespi, V. H.; Lopez-Urias, F.; Charlier, J. C.; Terrones, H.; Terrones, M. *Sci Rep* **2013,** 3, 1755.

19. Mak, K. F.; Lee, C.; Hone, J.; Shan, J.; Heinz, T. F. *Phys Rev Lett* **2010,** 105, (13), 136805.

20. del Corro, E.; Terrones, H.; Elias, A.; Fantini, C.; Feng, S. M.; Nguyen, M. A.; Mallouk, T. E.; Terrones, M.; Pimenta, M. A. *Acs Nano* **2014,** 8, (9), 9629-9635.

21. Scheuschner, N.; Ochedowski, O.; Schleberger, M.; Maultzsch, J. *Phys Status Solidi B* **2012,** 249, (12), 2644-2647.

22. Carvalho, B. R.; Malard, L. M.; Alves, J. M.; Fantini, C.; Pimenta, M. A. *Phys Rev Lett* **2015,** 114, (13), 136403.

23. Lee, J. U.; Park, J.; Son, Y. W.; Cheong, H. *Nanoscale* **2015,** 7, (7), 3229-3236.

24. Sun, L. F.; Yan, J. X.; Zhan, D.; Liu, L.; Hu, H. L.; Li, H.; Tay, B. K.; Kuo, J. L.; Huang, C. C.; Hewak, D. W.; Lee, P. S.; Shen, Z. X. *Phys Rev Lett* **2013,** 111, (12), 126801.

25. Sekine, T.; Nakashizu, T.; Toyoda, K.; Uchinokura, K.; Matsuura, E. *Solid State Commun* **1980,** 35, (4), 371-373.

26. Sekine, T.; Uchinokura, K.; Nakashizu, T.; Matsuura, E.; Yoshizaki, R. *J Phys Soc Jpn* **1984,** 53, (2), 811-818.

27. Sourisseau, C.; Cruege, F.; Fouassier, M.; Alba, M. *Chem Phys* **1991,** 150, (2), 281-293.

28. Terrones, H.; Del Corro, E.; Feng, S.; Poumirol, J. M.; Rhodes, D.; Smirnov, D.; Pradhan, N. R.; Lin, Z.; Nguyen, M. A. T.; Elias, A. L.; Mallouk, T. E.; Balicas, L.; Pimenta, M. A.; Terrones, M. *Sci Rep* **2014,** 4, 4215.

29. Livneh, T.; Spanier, J. E. *2d Mater* **2015,** 2, (3), 035003.

30. Renucci, J. B.; Tyte, R. N.; Cardona, M. *Phys Rev B* **1975,** 11, (10), 3885-3895.

31. Zhao, W. J.; Ghorannevis, Z.; Chu, L. Q.; Toh, M. L.; Kloc, C.; Tan, P. H.; Eda, G. *Acs Nano* **2013,** 7, (1), 791-797.

32. Gillet, Y.; Giantomassi, M.; Gonze, X. *Phys Rev B* **2013,** 88, (9), 094305.

33. Gutierrez, H. R.; Perea-Lopez, N.; Elias, A. L.; Berkdemir, A.; Wang, B.; Lv, R.; Lopez-Urias, F.; Crespi, V. H.; Terrones, H.; Terrones, M. *Nano Lett* **2013,** 13, (8), 3447-3454.

34. Gulans, A.; Kontur, S.; Meisenbichler, C.; Nabok, D.; Pavone, P.; Rigamonti, S.; Sagmeister, S.; Werner, U.; Draxl, C. *J Phys-Condens Mat* **2014,** 26, (36), 363202.

35. Gonze, X.; Amadon, B.; Anglade, P. M.; Beuken, J. M.; Bottin, F.; Boulanger, P.; Bruneval, F.; Caliste, D.; Caracas, R.; Cote, M.; Deutsch, T.; Genovese, L.; Ghosez, P.; Giantomassi, M.; Goedecker, S.; Hamann, D. R.; Hermet, P.; Jollet, F.; Jomard, G.; Leroux, S.; Mancini, M.; Mazevet, S.; Oliveira, M. J. T.; Onida, G.; Pouillon, Y.; Rangel, T.; Rignanese, G. M.; Sangalli, D.; Shaltaf, R.; Torrent, M.; Verstraete, M. J.; Zerah, G.; Zwanziger, J. W. *Comput Phys Commun* **2009,** 180, (12), 2582-2615.